

3D/2D Projected Shape Sensitivity Analysis of Total Joint Arthroplasty Implants

Andrew James Jensen, Scott Banks, Ph.D.

Abstract

Abstract Placeholder

Introduction

The application of Joint Track Machine Learning to reverse Total Shoulder Arthroplasty (rTSA) implants has unfolded a complex scenario. It highlights the intricate relationship between optimization algorithm performance, specific cost functions, and the inherent shape of the 3D models used for registration. A particular challenge lies in the intrinsic properties of humeral models, which present unique difficulties in model-image registration. To address these challenges, a thorough understanding of the relationship between a 3D shape and its projective geometry is crucial. This understanding is expected to shed light on the stark differences in algorithmic performance between total knee arthroplasty (TKA) and rTSA implants.

Understanding shape and its salient features has been a crucial aspect of computer vision since it was intertwined with psychology and neurology [1, 2]. Many intuitively appealing ideas about shape, such as the salience of curvature and vanishing points in projections, required mathematical definition to be effectively incorporated into image processing algorithms. Invariant Shape Descriptors, which remain consistent across rigid transformations or scaling, are particularly significant [26]. These descriptors encapsulate the essence of a shape, independent of factors like rotation, scaling, or position in an image. Normalized

Fourier Descriptors are among the most notable examples of invariant shape descriptors that have been used for aircraft recognition [25, 24, 22], aerial photography classification [17], model-image registration [27], and even measuring TKA kinematics from single-plane images [4]. Hu moments [11], the Hough Transform [3], Shape Context [7], Curvature scale space [14], the Angular Radial Transform [15], and multi-scale Shape Descriptors [23] have all been proposed as robust methods for vectorizing a shape into mathematically comparable elements.

The central inquiry of this chapter is whether a robust binary shape descriptor can elucidate the relative underperformance of model-image registration for rTSA implants compared to TKA implants. This question not only addresses a specific technical challenge but also aims to contribute to the broader understanding of shape analysis in medical imaging.

New Introduction

Understanding the in-vivo kinematics of total joint replacement has been a crucial factor in implant design, post-operative assessment, and predictive modeling for wear and failure patterns for nearly 30 years [10, 5, 6]. Recent advancements in computer vision and machine learning enabled these measurements to occur for total knee arthroplasty (TKA) in a fully autonomous and clinically practical setting utilizing single-plane fluoroscopy [8, 12]. Unfortunately, there are inherent limitations in using only a single camera, namely, the loss of depth perception and the introduction of ambiguous projected shapes during optimization [9, 18, 28, 4]. For mediolaterally symmetric tibial implants, this caused a phenomena dubbed “symmetry traps”, wherein two distinct 3D orientations of the implant would produce indistinguishable 2D projected geometry. Symmetry traps were solved by introducing a machine learning algorithm trained on true anatomic orientations that label and correct images that fell into such an optimization minima [13]. However, this solution still required that the symmetric implant optimize to one of the two potential local minima corresponding to the “symmetry trap”.

Unfortunately, when this same optimization routine and cost function [9, 12] was applied to reverse total shoulder arthroplasty (rTSA) it significantly underperformed compared to total knee arthroplasty implants. The optimization often failed in two ways. The first was error along the internal/external rotation axis, representing the axis of near-rotational

symmetry, as well as the axis whose features are most often occluded by the glenosphere implant in frontal-plane fluoroscopy. The second was a distal shift of the implant such that the local minima found properly registered the humeral stem, but not the humeral cup. This led to a deeper exploration of the psychology of shape [1, 2], which highlights the importance of relatively high curvature as being the most salient features in binary shape, and binary distance metrics [20, 21], which stresses the importance of fitting the cost-function metric to the problem at hand based on the underlying structure of your data.

To incorporate regions of high curvature into a novel-cost function, Menger’s discrete curvature algorithm [16] was applied to the contour of the projected implant shape. High curvature regions were selected algorithmically, and implemented in a *Modified Asymmetric Surface Distance*, using only the high-curvature keypoints as surface points (Eq. 1). Unfortunately, this too yielded sub-par results when applied to rTSA humeral implants, falling into the same errors as before.

$$J = \frac{\sum_{k \in \mathbb{K}} (\min_{p \in Proj} (p \cdot DM_k))}{N}$$

where

\mathbb{K} = Set of all keypoints (1)

N = Number of keypoints

DM_k = Distance map for keypoint k

p = Single point on projection silhouette

To improve the previously implemented Hamming Distance [12, 9], which is always maximally incorrect when there is no overlap, regardless of how close or far the estimate is, we introduce a *Modified Mean Surface Distance*. To do so, the element-wise multiplication of the projection estimate ($Proj_{x,y}$) and the distance map of the target ($DM_{x,y}$) is taken as a cost function (Eq. 2). This too, yielded sub-par performance.

$$J = \frac{\sum_{(x,y) \in Image} Proj_{x,y} DM_{x,y}}{\sum_{(x,y) \in Image} Proj_{x,y}} \quad (2)$$

Methods

Data Collection

First, we collected one manufacturer-provided model from each of: rTSA humeral implant, rTSA glenosphere implant, TKA femoral implant, and TKA tibial implant for testing shape sensitivity.

Image Generation

The binary silhouette of each implant was rendered using an in-house CUDA camera model (CUDA Version 12.1) [19] to a 1024×1024 image plane. The focal length of the pinhole camera model was 1000mm and each pixel was 0.3mm. All CUDA programming was performed on an NVIDIA Quadro P2200 GPU.

Invariant Angular Radial Transform

The invariant angular radial transform descriptor (IARTD) was selected due to its sensitivity in the radial direction [15]. This sensitivity allows us to address minor changes along the contour of our projected shape, which is a desirable property for determining the minor changes in shape with respect to input orientation.

The IARTD is a complex moment calculated by summing orthogonal basis components on the unit polar disk. Each basis function has an order (n) and a repetition (p). Intuitively, the order represents concentric “rings” in our polar disk, and the repetition is the number of “pie slices” in our unit disk along θ . To perform these calculations, we normalize our image such that $(0, 0)$ is at the center and $(\pm 1, \pm 1)$ are the four corners.

Each angular radial transform (ART) coefficient is a complex double integral (Eq. 3) over the image in polar coordinates, $f(\rho, \theta)$ multiplied by the ART basis function, $V_{np}(\rho, \theta)$ (Eq. 4).

$$F_{np} = \int_0^{2\pi} \int_0^1 f(\rho, \theta) V_{np}(\rho, \theta) \rho d\rho d\theta \quad (3)$$

$$V_{np}(\rho, \theta) = A_p(\theta)R_n(\rho) \quad (4)$$

Our radial basis function is comprised of a complex exponential, $A_p(\theta)$ (Eq. 5), which provides rotational invariance, and a trigonometric transform, $R_p(\theta)$ (Eq. 6) to provide orthogonality.

$$A_p(\theta) = \frac{1}{2\pi} e^{jp\theta} \quad (5)$$

$$R_n(\rho) = \begin{cases} 1 & n = 0 \\ 2 \cos(\pi n \rho) & n \neq 0 \end{cases} \quad (6)$$

Lastly, in order to correct for differences in the in-plane rotation, we apply a phase-correction to each ART coefficient (Eq. 7, Eq. 8).

$$\phi'_{np} = \phi_{np} - \phi_{n,1} \quad (7)$$

$$F'_{np} = F_{np} e^{-jp\phi_{n,1}} \quad (8)$$

And the, the final feature vector becomes a the polar decomposition of our coefficient at each order and repetition Eq. 9. We exclude values from the first two repetitions because they contain no valuable information. To construct the full IARTD feature vector, we used values of $n = \{0, \dots, 3\}$ and $p = \{0, \dots, 8\}$.

$$IARTD = \{|F'_{np}|, \phi'_{np}\} \text{ where } n \geq 0, p \geq 2 \quad (9)$$

Shape Differences and Sensitivity

The primary goal of this section is to establish a easily interpretable value that captures the overall change from one shape to another. For clarity in representation, successive rotations were denoted as subscripts, such that $R_z R_x R_y = R_{z,x,y}$. The application of the IARTD equation to an implant at a specific input orientation $R_{z,x,y}$ was represented as

$IARTD(R_{z,x,y})$. Shape differences were calculated using the central difference equation on the IARTD vector produced from two different orientations. The grid of sampled orientations had extrema of ± 30 with a step size of 5 for each of the x , y , and z axes. The “differences” along each axes were computed by applying a positive and negative rotation ($\pm\delta$) of 1 degree. And so, for every input x, y, z rotation, there will be three shape differences, one for each δ_x , δ_y or δ_z (Eq. 10). For notational brevity, we will condense the full equation down to a single $\Delta S(\delta)$, (representing $\Delta Shape$ for a differential rotation δ).

$$\Delta S(\delta)_{z,x,y} \equiv \frac{\partial IARTD(R_{z,x,y})}{\partial \delta} \propto IARTD(R_{z,x,y,+\delta}) - IARTD(R_{z,x,y,-\delta}) \quad (10)$$

Because each element of the IARTD vector is at a different scale, we must standardize each element in order to ensure accurate assessment of global behavior without analysis being dominated by a single value. We use z-score to do this, which assumes a normal distribution, but allows for some outliers if they are present.

After z-scaling, we took the Euclidean norm of each $S(\delta)_{z,x,y}$ to capture the total amount of change of that shape for a given differential rotation (Eq. 11). Our final step takes advantage of two factors: first, that our in-plane rotations are the first in our Euler sequence (z -axis), and second, that this type of rotation does not affect the in-plane shape. And so, for every x and y input rotation, we average all the values where x and y are held constant as z varies (Eq. 12). This yields our final values, which we will denote \mathbb{S} . $\mathbb{S}_{x,y}$ will have separate plots for each x , y , and z differential rotation and for each of the four implants. These plots will be compared with respect to JTML optimization performance and regions of difficulty for optimization.

$$\|S(\delta)_{z,x,y}\|_2 \quad (11)$$

$$\mathbb{S}(\delta)_{x,y} = \frac{\sum_z \|S(\delta)_{z,x,y}\|_2}{N} \quad (12)$$

Table 1: Average projected-shape sensitivity values for each of the implant models.

Implant Type	Average $\mathbb{S}(\delta_x)$	Average $\mathbb{S}(\delta_y)$	Average $\mathbb{S}(\delta_z)$
Humeral	8.83	4.82	7.08
Glenosphere	6.37	6.22	4.86
Femoral	6.88	8.68	4.93
Tibial	9.0	5.52	3.72

Results

The average value of $\mathbb{S}(\delta_y)$ for the humeral implant was much lower than all other implant types (Fig. 1) (Table 1). This rotation represents the final rotation in our Euler rotation sequence (Z-X-Y) and captures the internal/external rotation of the humeral implant. The average δ_x value for our humeral implant was the largest among all implants (Table 1). Additionally, the surface plotted by the humeral shape sensitivity for all $\delta_{x,y,z}$ is much smoother than any of the other plots, demonstrating the relative lack of shape difference for a wide range of input orientations. Many other plots had regions of relative in-sensitivity, like the glenosphere δ_y sensitivity along the $y = 0$ axis (Fig. 2) and the tibial δ_y sensitivity along the $x = 0$ axis (Fig. 4). The femoral implant had the highest average sensitivity ($\frac{\mathbb{S}(\delta_x) + \mathbb{S}(\delta_y) + \mathbb{S}(\delta_z)}{3}$) among all implant types .

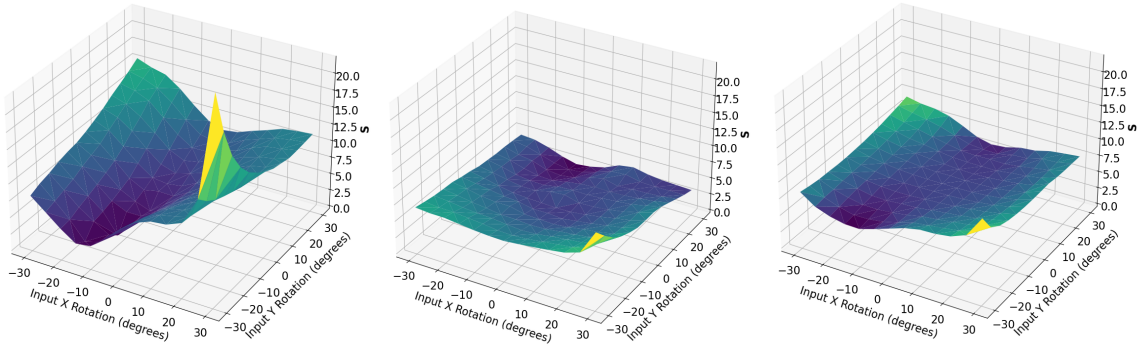


Figure 1: The \mathbb{S} plot for a humeral implant for δ rotations along the x, y, and z axis, respectively.

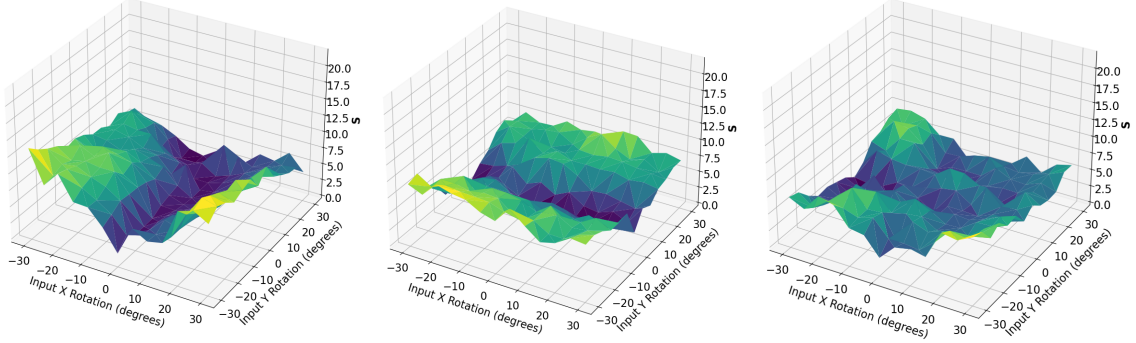


Figure 2: The \mathbb{S} plot for a glenosphere implant for δ rotations along the x, y, and z axis, respectively.

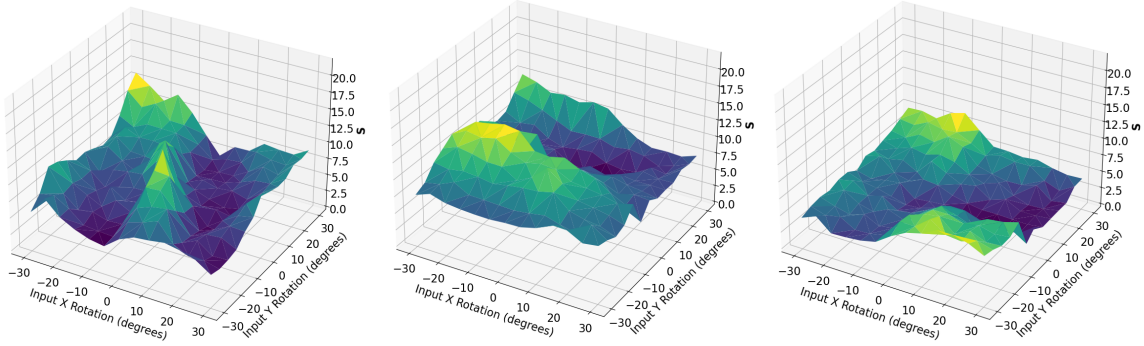


Figure 3: The \mathbb{S} plot for a femoral implant for δ rotations along the x, y, and z axis, respectively.

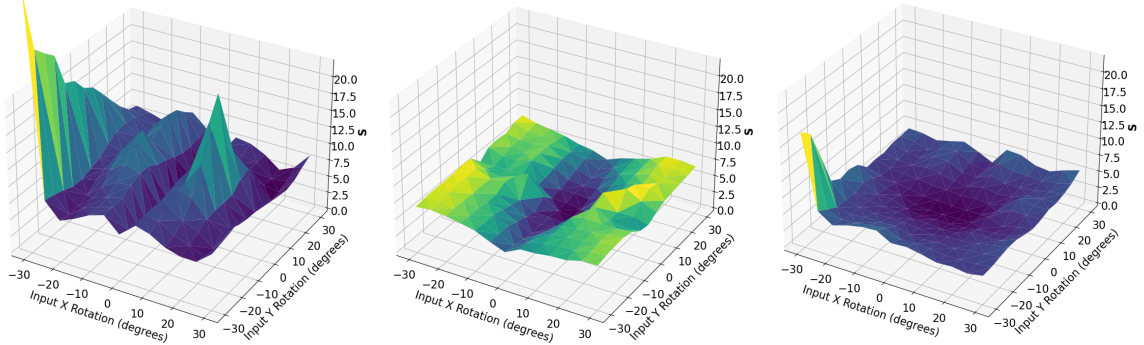


Figure 4: The \mathbb{S} plot for a tibial implant for δ rotations along the x, y, and z axis, respectively.

Discussion

The results shown align with many of our intuitive expectations about measuring the sensitivity of projected shape with respect to 3D object orientation, as well as aligned with the regions of difficulty for JTML optimization. The humeral implant demonstrated an overall

smooth and low shape sensitivity, especially for δ_y rotations (Table 1). This axis is the axis along which the humeral implant is the most cylindrical, which means that we would not expect to see a large change in the shape descriptor with minor δ_y rotations. Additionally, this is the axis which JTML had the most difficulty with.

We see similar intuitive results in the glenosphere implant, which had the lowest average $\mathbb{S}(\delta)$ value among all implant types. This bulk of the volume of this implant is the articulation surface, which closely resembles a sphere. Because the projection of a sphere (a circle) is unchanging with respect to the orientation of a sphere, we would expect that the more closely a shape resembles a sphere, then we should expect a lower overall shape sensitivity.

We see that the shape sensitivity of the tibial implant along the δ_y rotation corroborates our intuition about symmetry traps. Along the line defined by $x = 0$, we see a consistently low shape sensitivity. This internal/external rotation axis is exactly the axis that caused issues with symmetry traps, wherein 2 distinct 3D orientations produce the same projected shape. In the context of this discussion, we would say that the $\Delta S = 0$ between those two tibial orientations.

Another aspect of Joint Track Machine Learning that this study informs is the current use of Euler angles in our DIRECT-JTA optimization routine. Rather than independently varying all angles in a body-centered reference frame, which is insuitable for hyperbox creation, we are presently optimizing over a range of ordered rotations projected via the sequence $R_z R_x R_y$. As evidenced by the humeral implant’s struggles aligning the y -axis, this ordered sequence with a symmetric final axis can impede convergence.

Beyond the inherent shape sensitivities, such optimization limitations motivate exploring alternatives to Euler angles. Performing registration optimization directly on the Special Orthogonal group $SO(3)$ poses an intriguing direction. $SO(3)$ encapsulates all possible 3D rotations in a mathematically convenient structure (A *Lie Group*, which is both a manifold and a group). By optimizing on this manifold instead of using specific angle parametrizations, issues with gimbal lock and cascade effects can be avoided. Optimization over Lie groups is an emerging subfield - establishing robust $SO(3)$ -based registration cost functions could significantly improve JTML convergence while relying less on descriptor sensitivity along certain axes.

Conclusion

References

- [1] Fred Attneave. “Some Informational Aspects of Visual Perception.” In: *Psychological Review* 61.3 (1954), pp. 183–193. ISSN: 1939-1471, 0033-295X. DOI: 10.1037/h0054663. (Visited on 11/02/2023).
- [2] Fred Attneave and Malcolm D. Arnoult. “The Quantitative Study of Shape and Pattern Perception.” In: *Psychological Bulletin* 53.6 (Nov. 1956), pp. 452–471. ISSN: 1939-1455, 0033-2909. DOI: 10.1037/h0044049. (Visited on 11/02/2023).
- [3] D.H. Ballard. “Generalizing the Hough Transform to Detect Arbitrary Shapes”. In: *Pattern Recognition* 13.2 (Jan. 1981), pp. 111–122. ISSN: 00313203. DOI: 10.1016/0031-3203(81)90009-1. (Visited on 11/16/2023).
- [4] S.A. Banks and W.A. Hodge. “Accurate Measurement of Three-Dimensional Knee Replacement Kinematics Using Single-Plane Fluoroscopy”. In: *IEEE Transactions on Biomedical Engineering* 43.6 (June 1996), pp. 638–649. ISSN: 00189294. DOI: 10.1109/10.495283. (Visited on 03/22/2021).
- [5] Scott A. Banks and W.Andrew Hodge. “2003 Hap Paul Award Paper of the International Society for Technology in Arthroplasty”. In: *The Journal of Arthroplasty* 19.7 (Oct. 2004), pp. 809–816. ISSN: 08835403. DOI: 10.1016/j.arth.2004.04.011. (Visited on 05/13/2021).
- [6] Scott A. Banks et al. “Rationale and Results for Fixed-Bearing Pivoting Designs in Total Knee Arthroplasty”. In: *The Journal of Knee Surgery* 32.07 (July 2019), pp. 590–595. ISSN: 1538-8506, 1938-2480. DOI: 10.1055/s-0039-1679924. (Visited on 10/19/2023).
- [7] Serge Belongie, Jitendra Malik, and Jan Puzicha. “Shape Matching and Object Recognition Using Shape Contexts”. In: *IEEE TRANSACTIONS ON PATTERN ANALYSIS AND MACHINE INTELLIGENCE* 24.24 (2002).

- [8] Jordan S. Broberg et al. “Validation of a Machine Learning Technique for Segmentation and Pose Estimation in Single Plane Fluoroscopy”. In: *Journal of Orthopaedic Research* (Feb. 2023). ISSN: 0736-0266, 1554-527X. DOI: 10.1002/jor.25518. (Visited on 02/13/2023).
- [9] P. D. L. Flood and Scott A. Banks. “Automated Registration of 3-D Knee Implant Models to Fluoroscopic Images Using Lipschitzian Optimization”. In: *IEEE Transactions on Medical Imaging* 37.1 (2018), pp. 326–335. DOI: 10.1109/tmi.2017.2773398.
- [10] Benjamin J. Fregly et al. “Computational Wear Prediction of a Total Knee Replacement from in Vivo Kinematics”. In: *Journal of Biomechanics* 38.2 (Feb. 2005), pp. 305–314. ISSN: 00219290. DOI: 10.1016/j.jbiomech.2004.02.013. (Visited on 08/05/2021).
- [11] Ming-Kuei Hu. “Visual Pattern Recognition by Moment Invariants”. In: *IEEE Transactions on Information Theory* 8.2 (Feb. 1962), pp. 179–187. ISSN: 0018-9448. DOI: 10.1109/TIT.1962.1057692. (Visited on 11/29/2023).
- [12] Andrew J. Jensen et al. “Joint Track Machine Learning: An Autonomous Method of Measuring Total Knee Arthroplasty Kinematics From Single-Plane X-Ray Images”. In: *The Journal of Arthroplasty* 38.10 (May 2023), pp. 2068–2074. ISSN: 08835403. DOI: 10.1016/j.arth.2023.05.029. (Visited on 06/22/2023).
- [13] Andrew James Jensen et al. “Correcting Symmetric Implant Ambiguity in Measuring Total Knee Arthroplasty Kinematics from Single-Plane Fluoroscopy”. In: (In Review).
- [14] Jan J Koenderink and Andrea J Van Doorn. “Surface Shape and Curvature Scales”. In: *Image and Vision Computing* 10.8 (Oct. 1992), pp. 557–564. ISSN: 02628856. DOI: 10.1016/0262-8856(92)90076-F. (Visited on 11/02/2023).
- [15] Jong-Min Lee and Whoi-Yul Kim. “A New Shape Description Method Using Angular Radial Transform”. In: *IEICE Transactions on Information and Systems* E95.D.6 (2012), pp. 1628–1635. ISSN: 0916-8532, 1745-1361. DOI: 10.1587/transinf.E95.D.1628. (Visited on 11/21/2023).
- [16] J. C. Léger. *Menger Curvature and Rectifiability*. Apr. 1999. arXiv: math/9905212. (Visited on 01/10/2024).

- [17] C. C. Lin and R. Chellappa. “Classification of Partial 2-D Shapes Using Fourier Descriptors”. In: *IEEE Transactions on Pattern Analysis and Machine Intelligence* PAMI-9.5 (Sept. 1987), pp. 686–690. ISSN: 0162-8828. DOI: 10.1109/TPAMI.1987.4767963. (Visited on 10/25/2023).
- [18] M.R. Mahfouz et al. “A Robust Method for Registration of Three-Dimensional Knee Implant Models to Two-Dimensional Fluoroscopy Images”. In: *IEEE Transactions on Medical Imaging* 22.12 (Dec. 2003), pp. 1561–1574. ISSN: 0278-0062. DOI: 10.1109/TMI.2003.820027. (Visited on 03/22/2021).
- [19] John Nickolls et al. “Scalable Parallel Programming with CUDA”. In: *ACM Queue* 6.2 (Mar. 2008), pp. 40–53.
- [20] Annika Reinke et al. *Common Limitations of Image Processing Metrics: A Picture Story*. Aug. 2023. arXiv: 2104.05642 [cs, eess]. (Visited on 11/16/2023).
- [21] Annika Reinke et al. *Understanding Metric-Related Pitfalls in Image Analysis Validation*. Sept. 2023. arXiv: 2302.01790 [cs]. (Visited on 11/16/2023).
- [22] Charles W. Richard and Hooshang Hemami. “Identification of Three-Dimensional Objects Using Fourier Descriptors of the Boundary Curve”. In: *IEEE Transactions on Systems, Man, and Cybernetics* SMC-4.4 (July 1974), pp. 371–378. ISSN: 0018-9472, 2168-2909. DOI: 10.1109/TSMC.1974.5408458. (Visited on 10/25/2023).
- [23] Khaled Al-Thelaya et al. “InShaDe: Invariant Shape Descriptors for Visual 2D and 3D Cellular and Nuclear Shape Analysis and Classification”. In: *Computers & Graphics* 98 (Aug. 2021), pp. 105–125. ISSN: 00978493. DOI: 10.1016/j.cag.2021.04.037. (Visited on 10/25/2023).
- [24] Timothy P. Wallace and Owen R. Mitchell. “Analysis of Three-Dimensional Movement Using Fourier Descriptors”. In: *IEEE Transactions on Pattern Analysis and Machine Intelligence* PAMI-2.6 (1980), pp. 583–588. ISSN: 0162-8828. DOI: 10.1109/TPAMI.1980.6447707. (Visited on 03/04/2022).

- [25] Timothy P. Wallace and Paul A. Wintz. “An Efficient Three-Dimensional Aircraft Recognition Algorithm Using Normalized Fourier Descriptors”. In: *Computer Graphics and Image Processing* 13.2 (Jan. 1980), pp. 99–126. ISSN: 0146664X. DOI: 10.1016/S0146-664X(80)80035-9. (Visited on 03/04/2022).
- [26] Dengsheng Zhang and Guojun Lu. “Review of Shape Representation and Description Techniques”. In: *Pattern Recognition* 37.1 (Jan. 2004), pp. 1–19. DOI: 10.1016/j.patcog.2003.07.008.
- [27] Dominique Zosso et al. “Bi-Planar 2D-to-3D Registration in Fourier Domain for Stereoscopic x-Ray Motion Tracking”. In: *Medical Imaging*. Ed. by Joseph M. Reinhardt and Josien P. W. Pluim. San Diego, CA, Mar. 2008, p. 69140I. DOI: 10.1117/12.769469. (Visited on 09/09/2021).
- [28] S. Zuffi et al. “A Model-Based Method for the Reconstruction of Total Knee Replacement Kinematics”. In: *IEEE Transactions on Medical Imaging* 18.10 (Oct./1999), pp. 981–991. ISSN: 02780062. DOI: 10.1109/42.811310. (Visited on 09/01/2020).